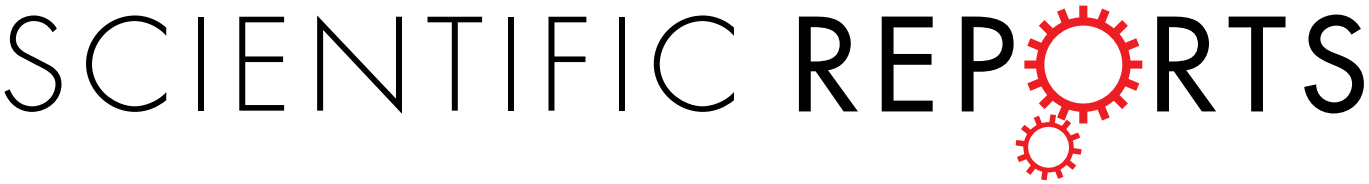

OPEN

A theoretical prediction of super high-performance thermoelectric materials based on MoS_2/WS_2 hybrid nanoribbons

Received: 24 August 2015
Accepted: 22 January 2016
Published: 17 February 2016

Zhongwei Zhang[1], Yuee Xie[1], Qing Peng[2] & Yuanping Chen[1]

Modern society is hungry for electrical power. To improve the efficiency of energy harvesting from heat, extensive efforts seek high-performance thermoelectric materials that possess large differences between electronic and thermal conductance. Here we report a super high-performance material of consisting of MoS_2/WS_2 hybrid nanoribbons discovered from a theoretical investigation using nonequilibrium Green's function methods combined with first-principles calculations and molecular dynamics simulations. The hybrid nanoribbons show higher efficiency of energy conversion than the MoS_2 and WS_2 nanoribbons due to the fact that the MoS_2/WS_2 interface reduces lattice thermal conductivity more than the electron transport. By tuning the number of the MoS_2/WS_2 interfaces, a figure of merit *ZT* as high as 5.5 is achieved at a temperature of 600 K. Our results imply that the MoS_2/WS_2 hybrid nanoribbons have promising applications in thermal energy harvesting.

Environmental pollution and energy shortages are two big concerns in modern society. Thermoelectric materials, which can convert waste heat in the environment to electricity, are expected to be helpful in resolving these two issues[1–4]. The energy conversion efficiencies of thermoelectric materials are measured by the so-called figure of merit *ZT* which is defined as $ZT = S^2\sigma T/k$, where *S* is the Seebeck coefficient, σ is the electronic conductance, and *k* ($k = k_e + k_p$) is the total thermal conductance including contributions of electrons (k_e) and phonons (k_p). Therefore, a high-performance thermoelectric material should have high electron conductance and low thermal conductance, i.e., electron crystals and thermal glasses. However, the *ZT* values of most bulk materials are very small (much less than 1.0) because their electronic and thermal properties always have the same trends[5–8].

There are extensive studies to search for high *ZT* materials. It is reported that the *ZT* values of some materials are improved significantly after nanocrystallization due to drastic changes of electronic and thermal properties[9–16]. For example, theoretical calculations proved that the *ZT* values of quasi-one nanowires have a larger increase than those of bulk and two-dimensional structures[2] nanostructured bismuth antimony telluride showed experimentally higher *ZT* values than the bulk because of a sharp reduction in k_p[6]. Beyond the intrinsic improvement, the *ZT* values of nanostructures can be further enhanced by various modifications, such as hybridization[10–12], doping[13,14], absorption[15,16], *etc*. Previous theoretical studies indicated that hybrid nanostructures, such as SiGe alloys and hybrid BN/graphene nanoribbons, possess higher thermoelectric properties than single nanostructures[11,12]. Even if the thermoelectric performances of nanostructures are much better than those of bulk, most of them still cannot meet the requirements for real world applications. As such, the search for high-performance thermoelectric materials for energy harvesting applications has become a main focus in the thermoelectric field.

Recently, the thermoelectric properties of single-layer or few-layer transition metal dichalcogenides (TMD) MX_2 (M = Mo, W, while X = S, Se *etc.*) have attracted attention[17–21]. MoS_2 and WS_2 are two typical TMDs, which are considered as excellent electronic materials because of direct band gaps and high carrier mobility. Electron transistors based on MoS_2 and WS_2 have been reported and show high electronic performance, while the thermal conductivities of the two nanosheets are relatively low[22–26]. Therefore, MoS_2 and WS_2 monolayer should have high *ZT* values, which have been proven by previous theoretical studies[18,19,21]. Meanwhile, some interesting MoS_2/WS_2

[1]School of Physics and Optoelectronics, Xiangtan University, Xiangtan 411105, Hunan, P.R. China. [2]Department of Mechanical, Aerospace and Nuclear Engineering, Rensselaer Polytechnic Institute, Troy, NY, 12180, USA. Correspondence and requests for materials should be addressed to Y.X. (email: xieyech@xtu.edu.cn) or Y.C. (email: chenyp@xtu.edu.cn)

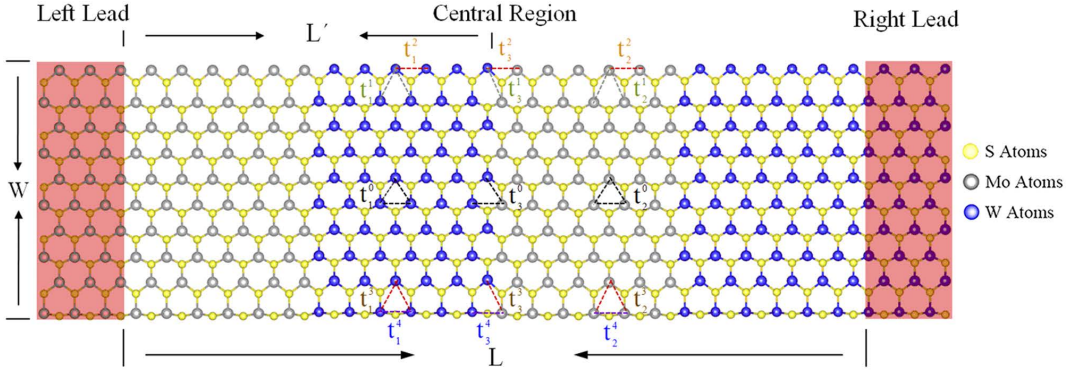

Figure 1. Atomic structures of zigzag-edge MoS_2/WS_2 hybrid nanoribbons. The model can be divided into three parts – a central scattering region and two (left and right) leads shown in the red boxes. The central scattering region, length L and width W, is a finite superlattice which consists of N periods. The length of each period is L', and thus $N = L/L'$ (here $N = 2$). $t_{\alpha=1,2,3}^{m=0,1,2,3,4}$ represents the hopping integrals between atoms, where the superscript 0 is set for internal atoms while others are set for edge atoms, and the subscripts 1, 2, and 3 are set for Mo-Mo, W-W, and Mo-W atoms, respectively.

hybrid nanostructures have been synthesized experimentally and studied theoretically[27–30]. However, the hybrid MoS_2/WS_2 nanoribbons have not been synthesized yet to the best of the authors' knowledge. Their thermoelectric properties are still unknown.

In this paper, thermoelectric transport in MoS_2/WS_2 hybrid nanoribbons is studied using nonequilibrium Green's function (NEGF) methods combined with first-principles and molecular dynamics methods[31–35]. The hybrid nanoribbons show high-performance thermoelectric properties compared to pure MoS_2 and WS_2 nanoribbons. Furthermore, the ZT values can be enhanced by modulating the number of interfaces in the structures, which approach 5.5 at 600 K and 4.0 at 300 K, respectively. The variations of the Seebeck coefficient, electronic, and thermal conductances are analyzed to interpret the enhanced thermoelectric properties. The super high ZT values indicate that the MoS_2/WS_2 hybrid nanoribbons are ideal high-performance thermoelectric materials with high energy conversion efficiencies.

Results and Discussion

The MoS_2/WS_2 hybrid nanostructures, as shown in Fig. 1, can be divided into three parts, one central scattering region and two (left and right) leads. The central region consists of finite periodic structures. Each period has one finite MoS_2 nanoribbon and one finite WS_2 nanoribbon. The two leads are semi-infinite MoS_2 or WS_2 nanoribbons. The length and width of the central region are labeled as L and W, respectively, and the length of a period of the central region is labeled as L'. Therefore, $L = N \times L'$, where N is the periodic number of the central scattering region.

A tight-binding (TB) Hamiltonian is used to describe the electronic properties of the hybrid structures,

$$H = \left(\sum_i \varepsilon_1 a_i^\dagger a_i + \sum_{ij} t_1 a_i^\dagger a_j\right) + \left(\sum_{i'} \varepsilon_2 b_{i'}^\dagger b_{i'} + \sum_{i'j'} t_2 b_{i'}^\dagger b_{j'}\right) + \sum_{ij'} t_3 a_i^\dagger b_{j'} \quad (1)$$

where the three terms represent the Hamiltonians of the MoS_2 nanoribbons, WS_2 nanoribbons, and their interactions, respectively. $t_{1,2}$ and $\varepsilon_{1,2}$ are the third-order hopping integrals for the nearest-neighbor atoms and site energies, which can be obtained from the GGA parameters in ref. 36. In ref. 36, the Hamiltonians of MoS_2 and WS_2 are described by three atomistic d orbitals of transition metal atoms, because the band edges mostly consist of d_{x^2}, d_{xy}, and $d_{x^2-y^2}$ orbitals, while the hopping integral t_3 for the interaction of Mo and W atoms are taken to be the average values of t_1 and t_2, i.e., $t_3 = \sqrt{t_1 \times t_2}$. To reflect the reconstruction of the ribbon edges, the hopping integrals are varied and reset as t_α^m ($m = 0, 1, 2, 3, 4,\ \alpha = 1, 2, 3$), where $m = 0$ for internal atoms and 1, 2, 3, and 4 are for edged atoms, as shown in Fig. 1. The values of t_α^m are inversely proportional to the corresponding bond lengths. According to the Hamiltonian in Eq. (1), we can use the NEGF method to calculate the electronic transport properties, including electronic conductance σ, Seebeck coefficient S, and electronic thermal conductance k_e. To verify the reliability of the TB parameters, we compare the electronic density of states (DOS) calculated by NEGF and density functional based tight binding (DFTB) methods[37,38]. The results indicate that the TB parameters can present the same energy gaps to those of the DFTB method, and the DOS profiles based on the TB parameters are also approximately similar to those of the DFTB method (see Fig. S1 in the Supplementary Information). For thermal transport properties, the phonon thermal conductance of the nanoribbons can be calculated using a harmonic approximation. One just needs to substitute the Hamiltonian matrix H by the mass-weighed force constant matrix K. Please see the Methods section for more details.

We calculate ZT as a function of chemical potential μ at $T = 300$ K for a MoS_2/WS_2 hybrid nanoribbon ($L = 8.37$ nm and $W = 2.34$ nm) where the central region only consists of one MoS_2/WS_2 interface, as shown in Fig. 2(a). The results for pure MoS_2 and WS_2 nanoribbons with the same size are also shown for comparison. It is

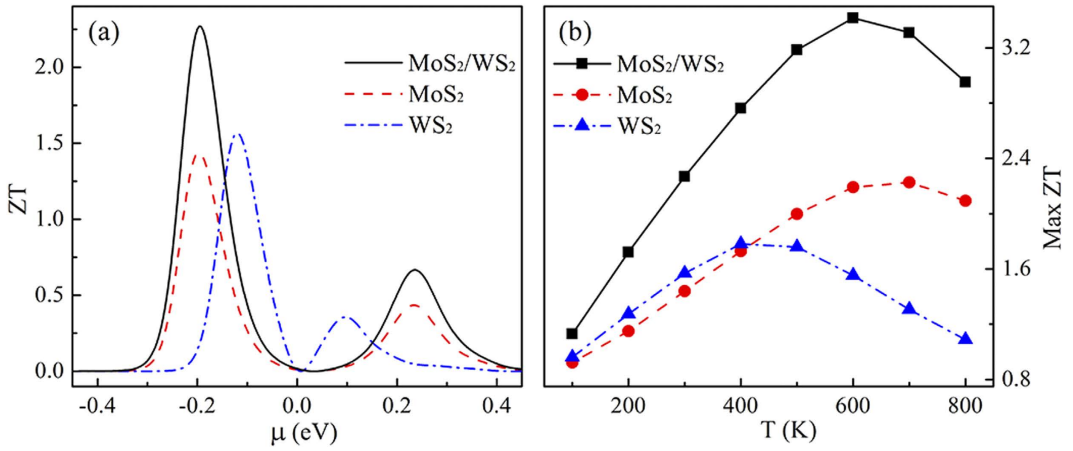

Figure 2. (**a**) *ZT* as a function of chemical potential μ for MoS_2/WS_2 ($N=1$), MoS_2, and WS_2 nanoribbons, respectively, at $T=300$ K. (**b**) The Max *ZT* value as a function of temperature for MoS_2/WS_2 ($N=1$), MoS_2, and WS_2 nanoribbons.

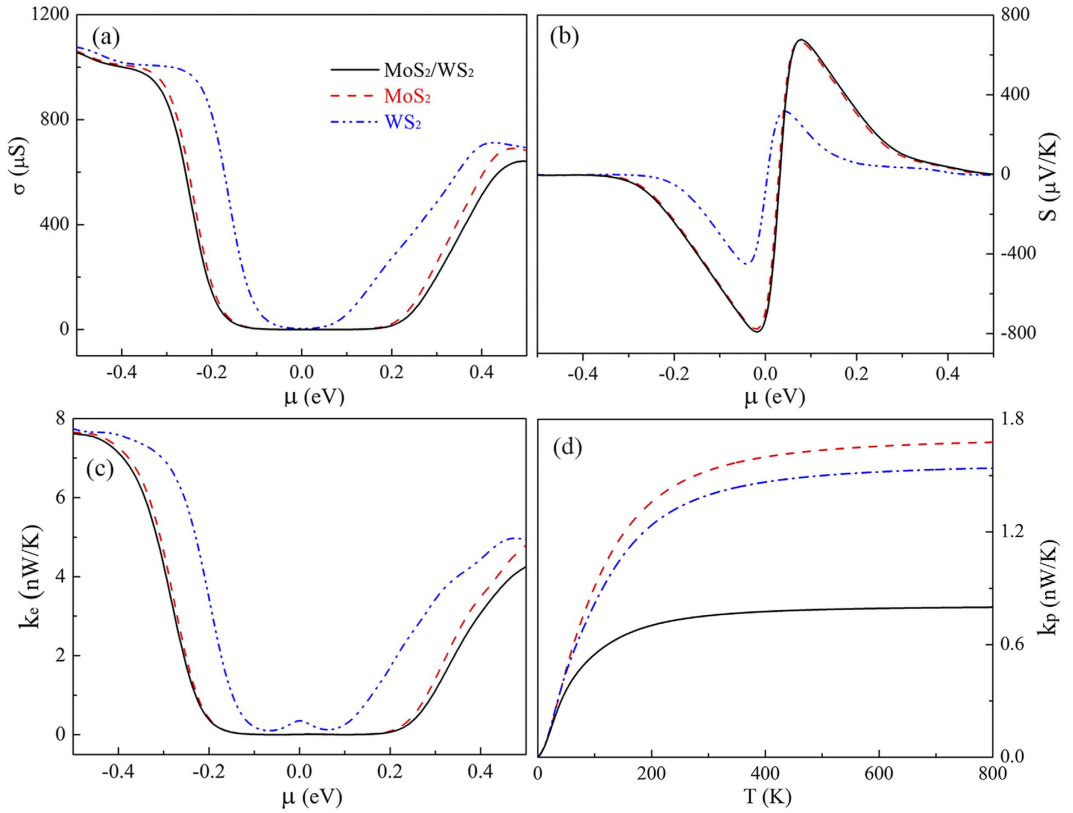

Figure 3. (**a**) σ, (**b**) *S*, and (**c**) k_e of MoS_2/WS_2 ($N=1$), MoS_2, and WS_2 nanoribbons as a function of chemical potential μ, respectively, at $T=300$ K. (**d**) k_p of MoS_2/WS_2 ($N=1$), MoS_2, and WS_2 nanoribbons as a function of temperature *T*.

found that the maximum values of *ZT* (Max *ZT*) for the three structures all appear at $\mu < 0$, moreover, the Max *ZT* of the MoS_2/WS_2 nanoribbon is larger than those of the two pure structures. The Max *ZT* of the hybrid nanoribbon is 2.3, while values for WS_2 and MoS_2 are 1.6 and 1.5, respectively. Therefore, after hybridization, *ZT* values of the pure nanoribbons are increased approximately by 1.5 times at room temperature.

The effect of temperature *T* on the Max *ZT* of the three structures is illustrated in Fig. 2(b). All of the *ZT* curves display the same trend—an increase at low temperature to the maximum followed by reduction at high temperature. With the variation of *T*, the highest *ZT* of the MoS_2/WS_2 hybrid nanoribbon appears at $T=600$ K with a value of 3.5 while the maximum values for the pure MoS_2 and WS_2 nanoribbons are only 2.3 (at 700 K) and 1.8 (at

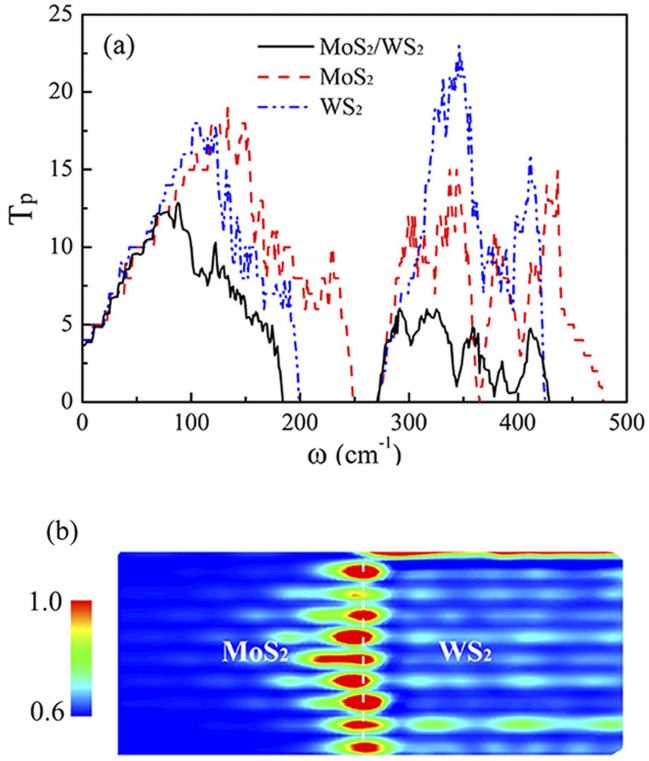

Figure 4. (**a**) Phonon transmission coefficient T_p of MoS_2/WS_2 ($N = 1$), MoS_2, and WS_2 nanoribbons as a function of frequency ω. (**b**) Phonon LDOS in the MoS_2/WS_2 ($N = 1$) nanoribbons at $\omega = 200.0$, 343.6, and 400.0 cm^{-1}. The color bar presents the strength of phonon localization.

400 K), respectively. Moreover, the ZT values of hybrid nanoribbons are higher than those of pure nanoribbons at any temperature. This further indicates that the hybridization enhances thermoelectric efficiency drastically.

To scrutinize the mechanism of the increment of ZT in hybrid structures over pure ones, we calculate their electronic and thermal properties, such as σ, S, k_e, and T_p. Equations (2–4) demonstrate that σ, S, and k_e are functions of chemical potential μ and temperature T, while k_p is only a function of temperature T. Figure 3(a–c) show σ, S, and k_e as a function of μ for the three structures at $T = 300$ K. Seen from Fig. 3(a), the σ curve of the WS_2 nanoribbon is somewhat similar to that of the MoS_2 nanoribbon, except the threshold values of the latter are smaller than that of the former, which is mainly because the band gap of the WS_2 nanoribbon is smaller than that of the MoS_2 nanoribbon. For the MoS_2/WS_2 hybrid nanoribbon, its energy gap should be equal to the wider one, i.e., equal to that of MoS_2 nanoribbon. The results of DFTB calculation further confirm this point (see Fig. S1 in the Supplementary Information). Therefore, the σ curve of the hybrid nanoribbon has the same threshold as that of the MoS_2 nanoribbon. Meanwhile, the interface scattering to the electrons is weak due to the similarity of the electronic properties of MoS_2 and WS_2, and thus σ values of the hybrid nanoribbon are just a little smaller than those of the pure nanoribbons. The maximum S usually depends linearly on the band gap[39,40], therefore, one can see from Fig. 3(b) that the S values of hybrid and MoS_2 nanoribbons are larger than that of WS_2 nanoribbons. The electronic thermal conductance k_e shown in Fig. 3(c) almost coincides with the behavior of electron conductance σ, because both of them are attributed to the contribution of electrons. Figure 3(d) presents another ZT factor, the phononic thermal conductance k_p as a function of T. The MoS_2 nanoribbon exhibits a higher k_p than the WS_2 nanoribbon while the k_p of the MoS_2/WS_2 hybrid nanoribbon is the lowest, which is only about 0.5 times that of WS_2 and MoS_2 nanoribbons. From these results, one can find that the improved ZT value of the hybrid nanoribbon is mainly originated from the sharp decrease of phononic thermal conductance k_p while the effect of the interface on σ, S, and k_e is relatively small.

In order to understand the drop of k_p in the hybrid structure, we compare the phonon transmissions $T_p(\omega)$ in the MoS_2, WS_2, and hybrid nanoribbons, as shown in Fig. 4(a). The comparison reveals that two reasons cause the drop of k_p in the hybrid structure. One is the shrinkage of the spectrum ranges where have effective phonon transmission. For example, the gaps between acoustical and optical phonons for MoS_2 and WS_2 nanoribbons are 24 and 73 cm^{-1}, respectively, while that for hybrid nanoribbon is 87 cm^{-1}. The other is the reduction of the transmission coefficients T_p. One can find that, as $\omega > 80$ cm^{-1}, T_p of all phonons in the hybrid structure are smaller than those in the pure nanoribbons. The two aspects demonstrate that the interface in the hybrid nanoribbon vastly weaken the phonon transport. The LDOS in the hybrid structures in Fig. 4(b) further illustrates this point. There are many localized phonons at the interface, which acts as a potential barrier blocking the phonons from left to right. It is noted that the phonon localization at the nanoribbon edges is small although the edges are unpassivated. We also compare thermal conductances of nanoribbons with different types of edges, such as unpassivated,

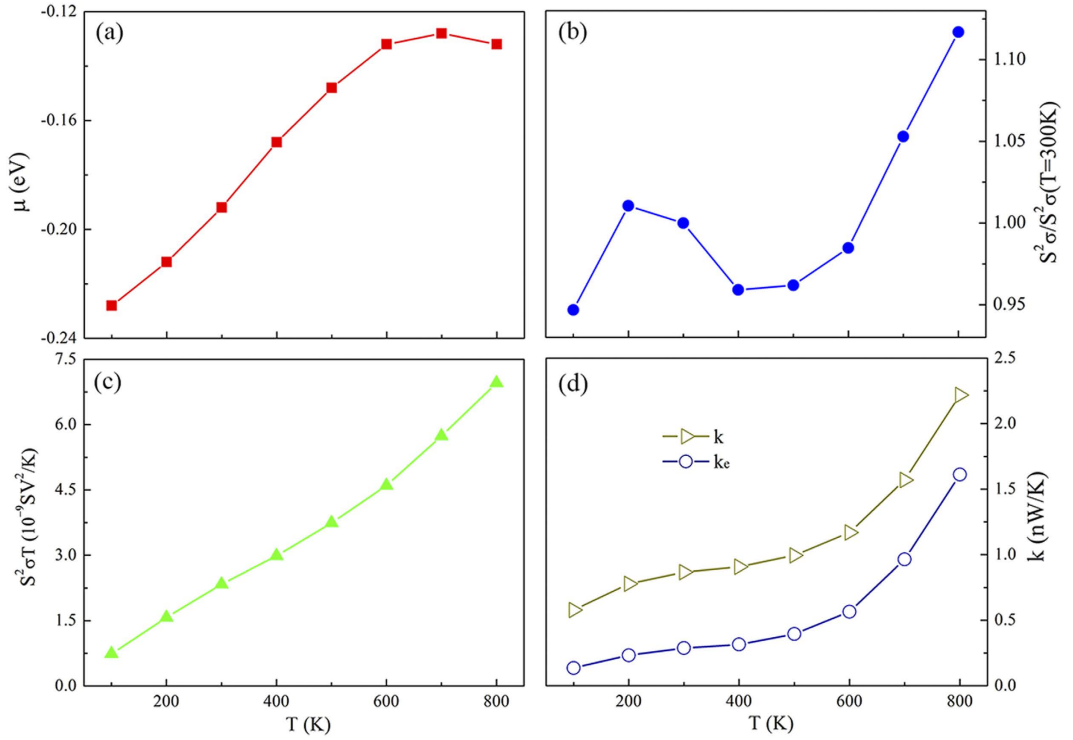

Figure 5. (**a**) μ, (**b**) $S^2\sigma$, (**c**) $S^2\sigma T$ and (**d**) k, ke of MoS_2/WS_2 ($N=1$) nanoribbons as a function of temperature T, corresponding to Max ZT in Fig. 2(b). The $S^2\sigma$ is normalized by the $S^2\sigma$ at $T=300$ K, $S^2\sigma/S_0{}^2\sigma_0$ ($T=300$K).

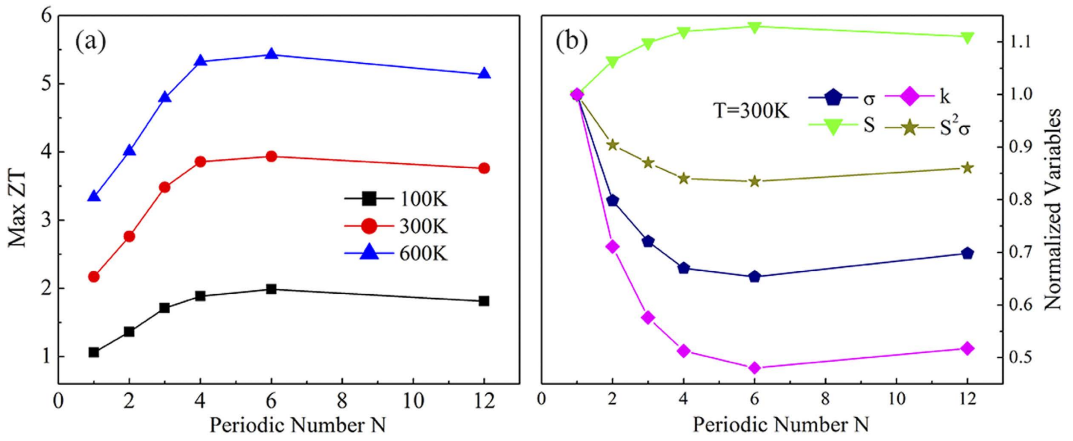

Figure 6. (**a**) The Max ZT value of the MoS_2/WS_2 hybrid nanoribbon as a function of periodic number N, at $T=100$ K, 300 K, and 600 K. (**b**) Normalized variables σ, S, k, and $S^2\sigma$ as a function of periodic number N, at $T=300$ K. The values are normalized by the values for $N=1$.

S-half passivated[41,42] and periodic edges (see Fig. S2(c) in the Supplementary Information). The results indicate that the effect of dangling bonds, phonon localization, and scattering at the edges on the thermal transport is very weak.

To analyze the effect of temperature T on the Max ZT of the MoS_2/WS_2 hybrid nanoribbon, we calculate the variations of μ, $S^2\sigma$, $S^2\sigma T$, and k (k_e) corresponding to the Max ZT under temperature T, as shown in Fig. 5. It is seen from Fig. 5(a) that the chemical potential μ gradually shifts to the Fermi level with the increase of T. The variation of thermopower $S^2\sigma$ in Fig. 5(b) is irregular due to the different chemical potential μ and the small amplitude of variation, indicating the effect of temperature T on the thermopower is weak. This is further proved by the nearly linear relation between $S^2\sigma T$ and T in Fig. 5(c). Therefore, the effect of temperature T on the Max ZT is determined by the relation of thermal conductance k and T. The total thermal conductance k is composed of electronic thermal conductance k_e and phononic thermal conductance k_p. These three quantities as a function

of temperature are plotted in Fig. 5(d) for comparison. The total thermal conductance k increases slowly with the temperature as $T < 600$ K and then increases rapidly as $T > 600$ K, which is induced by the sharp increase of k_e after $T > 600$ K. The variation of k_e with T is related to the shift of chemical potential μ and the Fermi distribution. As a result, the highest ZT value appears at $T = 600$ K. Because the MoS_2/WS_2 interface reduces the phononic thermal conductance significantly with small penalty on other components, we can further increase the ZT by introducing more interfaces in the system. This could be achieved by enlarging the spatial frequencies of interfaces, which is equivalent to period number N while the total length is fixed. Figure 6(a) shows Max ZT values for MoS_2/WS_2 hybrid nanoribbons whose central scattering region includes N periods (N units of MoS_2/WS_2). The length L of the hybrid nanoribbons is fixed at 8.37 nm, and thus the increase in periodic number N represents the corresponding decrease of the periodic length L'. One can find that the Max ZT increases with N as $N < 6$, and then decreases as N further increases. The highest ZT exists at $N = 6$, and the values at $T = 100$, 300, and 600 K are 2.0, 4.0, and 5.5, respectively, which are 2 ~ 3 times those of pure WS_2 and MoS_2 nanoribbons. Obviously, the multi-periodic hybrid structures further enhance the thermoelectric properties.

To examine the effect of periodic number N on ZT as well as its components, we study the normalized σ, S, $S^2\sigma$, and k for multi-periodic hybrid nanoribbons at $T = 300$ K. They vary as a function of the periodic number N, as shown in Fig. 6(b). The normalized σ and k decrease as N increases and $N < 4$. This is because the number of the interfaces in the central scattering region increases with the periodic number N, which strengthens the scattering of electrons and phonons and thus σ and k decrease. As discussed above, the effect of the interfaces on the phonon transport is larger than that on the electron transport, and thus the decrease speed of k is faster. As $N > 4$, the central region gradually becomes a super lattice, therefore σ and k decrease slowly at first and then increase with N. On the other hand, the variation of S is inversely proportional to that of σ and k. It increases with N as $N < 4$ and then decreases slowly. The variation of $S^2\sigma$ with N is small, indicating that the improved ZT values for the multi-periodic structures are still originated from the sharp decrease of k.

As mentioned above, in-plane lateral hybrid MoS_2/WS_2 heterojunctions have been synthesized by ambient-pressure chemical vapor deposition (CVD) and single-step vapor phase growth[27,28]. Therefore, the hybrid MoS_2/WS_2 nanoribbons with one interface ($N = 1$) in Fig. 1 can be obtained by cutting these two-dimensional heterojunctions[43]. Although the hybrid MoS_2/WS_2 heterojunctions with multiple interfaces have not been reported up to date, these heterojunctions are expected to be synthesized in the near future, by following the similar synthetic process of periodic BN/graphene heterostructures created by lithography patterning and sequential CVD growth steps[44]. Then, the hybrid MoS_2/WS_2 nanoribbons with periodic interfaces can also be obtained. The high-performance thermoelectric properties of these hybrid nanoribbons make them have promising applications in thermal energy harvesting.

Summary

In summary, we study thermoelectric properties of MoS_2/WS_2 hybrid nanoribbons, by using the NEGF method combined with first-principles and molecular dynamics methods. The hybrid nanoribbons exhibit super high thermoelectric properties. With the drastic reduction of k_p and little change in the electronic properties, the maximum ZT of the hybrid nanoribbon with one interface is increased to 1.5 ~ 2 times that of pure nanoribbons. Moreover, the ZT values can be further increased by modulating the interface number. The highest ZT value of hybrid nanoribbons can approach 4.0 at 300 K and 5.5 at 600 K. Therefore, MoS_2/WS_2 hybrid nanoribbons are very promising materials for high-performance thermoelectric devices.

Methods

In this section we have outlined some key steps in applying the NEGF approach for the electronic and phononic transport. We can use the NEGF method to calculate the electronic transmission coefficient $T_e[E] = Tr\{G^r(E)\Gamma_L G^a(E)\Gamma_R\}$[45,46], where $G^r(E)$ and $G^a(E) = [G^r(E)]^\dagger$ are the retarded and advanced Green's functions which included the two leads' effects, and $\Gamma_{\beta=L,R} = i(\sum_\beta^\gamma - \sum_\beta^a) = -2ImV^{C\beta}g_\beta^\gamma V^{\beta C}$ is the coupling function of the β lead. Then the electronic conductance σ, Seebeck coefficient S, and electronic thermal conductance k_e can be calculated based on the Onsager's relations and Landauer's theory of quantum transport:[5,11,33]

$$\sigma(\mu, T) = e^2 L_0(\mu, T), \tag{2}$$

$$S(\mu, T) = \frac{1}{eT}\frac{L_1(\mu, T)}{L_0(\mu, T)}, \tag{3}$$

$$k_e(\mu, T) = \frac{1}{T}\left[L_2(\mu, T) - \frac{L_1(\mu, T)^2}{L_0(\mu, T)}\right], \tag{4}$$

where $L_n(\mu, T) = \frac{2}{h}\int_{-\infty}^{+\infty}(E-\mu)^n\left[-\frac{\partial f_e(E,\mu,T)}{\partial T}\right]T_e[E]dE$ is the Lorenz integral and $f_e(E, \mu, T)$ is the Fermi-Dirac distribution function at the chemical potential μ and temperature T.

Thermal transport properties of the hybrid nanoribbons can be calculated as follow. At first, the Stillinger-Weber (SW) potential[47] parameters used to describe the interatomic interactions in the hybrid nanoribbons can be obtained by the software GULP based on molecular dynamics scheme[48,49]. These parameters can fit well the phonon dispersions calculated by the first-principles method. Then, the force constants matrices K of the hybrid structures can be also obtained by GULP according to the potentials. In the GULP, the force constant is

given by the second derivatives with respect to the potential energy, and thus they only include the harmonic components. The detailed procedures for dealing with the potential parameters and force constants can be found in the Supporting Information. After K is obtained, the phonon transmission coefficient $T_p(\omega)$ can be calculated, according to the NEGF procedure in analogy to that of calculating electronic transmission coefficient[34,35,50,51]. Finally, the lattice thermal conductance is given by $k_p(T) = \frac{h}{4\pi^2}\int_0^\infty \frac{\partial f_p(\omega)}{\partial T} T_p(\omega)\omega d\omega$, where $f_p(\omega)$ is the Bose-Einstein distribution function for heat carriers. We have therefore all the ingredients required to calculate ZT. Meanwhile, the LDOS at site j: $LDOS_j(\omega) = i\omega\left(G^r_{jj} - G^a_{jj}\right)/\pi$ can also be calculated.

References

1. Venkatasubramanian, R., Siivola, E., Colpitts, T. & O'Quinn, B. Thin-film thermoelectric devices with high room-temperature figures of merit. *Nature* **413,** 597–602 (2001).
2. Hicks, L. D. & Dresselhaus, M. S. Effect of quantum-well structures on the thermoelectric figure of merit. *Phys. Rev. B* **47,** 12727–12731 (1993).
3. Yang, N., Xu, X., Zhang, G. & Li, B. Thermal transport in nanostructures. *AIP Adv.* **2,** 041410 (2012).
4. Harman, T. C., Taylor, P. J., Walsh, M. P. & LaForge, B. E. Quantum dot superlattice thermoelectric materials and devices. *Science* **297,** 2229–2232 (2002).
5. Wang, B., Zhou, J., Yang, R. & Li, B. Ballistic thermoelectric transport in structured nanowires. *New J. Phys.* **16,** 065018 (2014).
6. Poudel, B. *et al.* High-thermoelectric performance of nanostructured bismuth antimony telluride bulk alloys. *Science* **320,** 634–638 (2008).
7. Snyder, G. J. & Toberer, E. S. Complex thermoelectric materials. *Nat. Mater.* **7,** 105–114 (2008).
8. Minnich, A. J., Dresselhaus, M. S., Ren, Z. F. & Chen, G. Bulk nanostructured thermoelectric materials: current research and future prospects. *Energy & Envir. Sci.* **2,** 466–479 (2009).
9. Shelley, M. & Mostofi, A. A. Prediction of high ZT in thermoelectric silicon nanowires with axial germanium heterostructures. *Euro. Phys. Lett.* **94,** 67001 (2011).
10. Wang, N. *et al.* A novel high-performance photovoltaic–thermoelectric hybrid device. *Energy & Envir. Sci.* **4,** 3676–3679 (2011).
11. Yang, K. K. *et al.* Enhanced thermoelectric properties in hybrid graphene/boron nitride nanoribbons. *Phys. Rev. B* **86,** 045425 (2012).
12. Minnich, A. J. *et al.* Modeling study of thermoelectric SiGe nanocomposites. *Phys. Rev. B* **80,** 155327 (2009).
13. Ohta, S., Nomura, T., Ohta, H. & Koumoto, K. High-temperature carrier transport and thermoelectric properties of heavily La-or Nb-doped SrTiO3 single crystals. *J. Appl. Phys.* **97,** 034106 (2005).
14. Ohta, S. *et al.* Large thermoelectric performance of heavily Nb-doped SrTiO 3 epitaxial film at high temperature. *Appl. Phys. Lett.* **87,** 092108 (2005).
15. Bansal, P. & Martin, A. Comparative study of vapour compression, thermoelectric and absorption refrigerators. *Int. J. Energy Res.* **24,** 93–107 (2000).
16. Riffat, S. & Qiu, G. Comparative investigation of thermoelectric air-conditioners versus vapour compression and absorption air-conditioners. *Appl. Therm. Eng.* **24,** 1979–1993 (2004).
17. Wickramaratne, D., Zahid, F. & Lake, R. K. Electronic and thermoelectric properties of few-layer transition metal dichalcogenides. *J. Chem. Phys.* **140,** 124710 (2014).
18. Lee, C., Hong, J., Whangbo, M. H. & Shim, J. H. Enhancing the Thermoelectric Properties of Layered Transition-Metal Dichalcogenides 2H-MQ2(M = Mo, W; Q = S, Se, Te) by Layer Mixing: Density Functional Investigation. *Chem. Mater.* **25,** 3745–3752 (2013).
19. Fan, D. D. *et al.* MoS_2 nanoribbons as promising thermoelectric materials. *Appl. Phys. Lett.* **105,** 133113 (2014).
20. Guo, H. *et al.* High pressure effect on structure, electronic structure, and thermoelectric properties of MoS_2. *J. Appl. Phys.* **113,** 013709 (2013).
21. Huang, W., Da, H. & Liang, G. Thermoelectric performance of MX2 (M = Mo,W; X = S,Se) monolayers. *J. Appl. Phys.* **113,** 104304 (2013).
22. Baugher, B. W., Churchill, H. O., Yang, Y. & Jarillo-Herrero, P. Intrinsic electronic transport properties of high-quality monolayer and bilayer MoS_2. *Nano Lett.* **13,** 4212–4216 (2013).
23. Splendiani, A. *et al.* Emerging photoluminescence in monolayer MoS_2. *Nano Lett.* **10,** 1271–1275 (2010).
24. Sahoo, S. *et al.* Temperature-Dependent Raman Studies and Thermal Conductivity of Few-Layer MoS_2. *J. Chem. Phys. C* **117,** 9042–9047 (2013).
25. Gu, X. & Yang, R. Phonon transport in single-layer transition metal dichalcogenides: A first-principles study. *Appl. Phys. Lett.* **105,** 131903 (2014).
26. Peng, Q. & De, S. Outstanding mechanical properties of monolayer MoS_2 and its application in elastic energy storage. *Phys. Chem. Chem. Phys.* **15,** 19427–19437 (2013).
27. Gong, Y. *et al.* Vertical and in-plane heterostructures from WS_2/MoS_2 monolayers. *Nat. Mater.* **13,** 1135–1142 (2014).
28. Zhang, X. Q. *et al.* Synthesis of lateral heterostructures of semiconducting atomic layers. *Nano Lett.* **15,** 410–415 (2015).
29. Wang, Q., Wu, P., Cao, G. & Huang, M. First-principles study of the structural and electronic properties of MoS_2–WS_2 and MoS_2–MoTe2 monolayer heterostructures. *J. Phy. D: Appl. Phys.* **46,** 505308 (2013).
30. Zhou, Y., Dong, J. & Li, H. Electronic transport properties of in-plane heterostructures constructed by MoS_2 and WS_2 nanoribbons. *RSC Adv.* **5,** 66852–66860 (2015).
31. Ouyang, Y. & Guo, J. A theoretical study on thermoelectric properties of graphene nanoribbons. *Appl. Phys. Lett.* **94,** 263107 (2009).
32. Markussen, T., Jauho, A. P. & Brandbyge, M. Electron and phonon transport in silicon nanowires: Atomistic approach to thermoelectric properties. *Phys. Rev. B* **79,** 035415 (2009).
33. Ouyang, T. & Hu, M. Thermal transport and thermoelectric properties of beta-graphyne nanostructures. *Nanotechnol.* **25,** 245401 (2014).
34. Yamamoto, T. & Watanabe, K. Nonequilibrium Green's Function Approach to Phonon Transport in Defective Carbon Nanotubes. *Phys. Rev. Lett.* **96,** 255503 (2006).
35. Mingo, N. Anharmonic phonon flow through molecular-sized junctions. *Phys. Rev. B* **74,** 125402 (2006).
36. Liu, G. B. *et al.* Three-band tight-binding model for monolayers of group-VIB transition metal dichalcogenides. *Phys. Rev. B* **88,** 085433 (2013).
37. Aradi, B., Hourahine, B. & Frauenheim, T. DFTB+, a Sparse Matrix-Based Implementation of the DFTB Method†. *J. Phys. Chem. A* **111,** 5678–5684 (2007).
38. Pecchia, A., Penazzi, G., Salvucci, L. & Di Carlo, A. Non-equilibrium Green's functions in density functional tight binding: method and applications. *New J. Phys.* **10,** 065022 (2008).
39. Goldsmid, H. & Sharp, J. Estimation of the thermal band gap of a semiconductor from Seebeck measurements. *J. Electr. Mater.* **28,** 869–872 (1999).
40. Kudo, A., Yanagi, H., Hosono, H. & Kawazoe, H. SrCu2O2: A p-type conductive oxide with wide band gap. *Appl. Phys. Lett.* **73,** 220–222 (1998).

41. Erdogan, E., Popov, I. H., Enyashin, A. N. & Seifert, G. Transport properties of MoS_2 nanoribbons: edge priority. *Eur. Phys. J. B* **85,** 33 (2012).
42. Li, Y. *et al.* Enhanced Li Adsorption and Diffusion on MoS_2 Zigzag Nanoribbons by Edge Effects: A Computational Study. *J. Phys. Chem. Lett.* **3,** 2221–2227 (2012).
43. Castellanos-Gomez, A. *et al.* Laser-thinning of MoS_2: on demand generation of a single-layer semiconductor. *Nano Lett.* **12,** 3187–3192 (2012).
44. Liu, Z. *et al.* In-plane heterostructures of graphene and hexagonal boron nitride with controlled domain sizes. *Nat. Nanotechnol.* **8,** 119–124 (2013).
45. Chen, Y. P., Xie, Y. E. & Yan, X. H. Resonant transmission via magnetically bound states in periodic quantum structures. *Phys. Rev. B* **76,** 115439 (2007).
46. Chen, Y. P., Xie, Y. E. & Yan, X. H. (n−2)-fold resonant splitting in open periodic quantum structures. *Phys. Rev. B* **74,** 035310 (2006).
47. Jiang, J. W., Park, H. S. & Rabczuk, T. Molecular dynamics simulations of single-layer molybdenum disulphide MoS_2: Stillinger-Weber parametrization, mechanical properties, and thermal conductivity. *J. Appl. Phys.* **114,** 064307 (2013).
48. Gale, J. D. & Rohl, A. The general utility lattice program. *Mol. Sim.* **29,** 291–341 (2003).
49. Gale, J. D. GULP: A computer program for the symmetry-adapted simulation of solids. *J. Chem. Soci., Faraday Trans.* **93,** 629–637 (1997).
50. Ouyang, T. *et al.* Thermal transport in hexagonal boron nitride nanoribbons. *Nanotechnol.* **21,** 245701 (2010).
51. Ouyang, T. *et al.* Thermal conductance modulator based on folded graphene nanoribbons. *Appl. Phys. Lett.* **99,** 233101 (2011).

Acknowledgements

This work was supported by the National Natural Science Foundation of China (Nos. 51176161, 51376005 and, 11474243).

Author Contributions

Z.W.Z., Y.E.X. and Y.P.C. established the theoretical models and supervised the project, Z.W.Z., Y.E.X. and Y.P.C. performed the calculations and data analysis, Z.W.Z. and Y.P.C. wrote the paper, Q.P. and Y.P.C. revised the paper.

Additional Information

Supplementary information accompanies this paper at http://www.nature.com/srep

Competing financial interests: The authors declare no competing financial interests.

How to cite this article: Zhang, Z. *et al.* A theoretical prediction of super high-performance thermoelectric materials based on MoS_2/WS_2 hybrid nanoribbons. *Sci. Rep.* **6**, 21639; doi: 10.1038/srep21639 (2016).